Detailed QM/MM study of the Electron Paramagnetic Resonance Parameters of Nitrosyl Myoglobin

Mahesh Sundararajan[†] and Frank Neese*

Max-Planck Institutfür Bioanorganische Chemie, Stiftstrasse 32-34, D-45470 Mülheim an der Ruhr, Germany

S *Supporting Information*

ABSTRACT: A number of popular density functionals are calibrated against high-resolution EPR data for low spin iron-nitrosyls present in nitric oxide bound myoglobin. The model incorporates both electrostatic and steric effects using a combined quantum mechanics/molecular mechanics (QM/MM) approach. Compared to the most recent experimental data, the calculated EPR parameters using GGA functionals are distinctly more accurate than those predicted by hybrid functionals. The latter is related to an erroneous spin distribution predicted with hybrid functionals in this particular case. However, owing to the inaccuracies in the prediction of spin state energetics, GGA functionals overestimate the binding energy of the nitric oxide ligand to the heme center. Using the calculated magnetic resonance parameters as well as the calculated rotational potential energy surface of the NO ligand over the heme plane, a possible geometric structure of elusive A-form if nitrosyl-myoglobin is proposed.

■ INTRODUCTION

Proteins involving heme iron centers are an important class of metalloproteins where many important physical, chemical and biological processes take place. The specific function of heme proteins is finely controlled in biology through the choice of the axial ligand(s) and the overall construction of the binding pocket.[1] In addition to the variability in oxidation and spin state of the central metal (apparently exclusively iron in nature) another degree of freedom is the oxidation state of the porphyrin itself which can act as a noninnocent ligand.[2] The binding of nitric oxide ((NO), another noninnocent ligand) to heme systems has attracted considerable attention (Figure 1).[3−6] Initially, NO was used as a "magnetic probe" of O_2 binding.[7−12]

Besides the heme and NO groups, the active site of MbNO consists of two histidine residues (His93 and His64) and one valine (Val68) residue anchoring the NO (Figure 1).[13,14] The proximal ligand is His93 and in the distal binding pocket His64 is located in close proximity to the bound NO group. Furthermore, the active site contains Val68, which may be involved in hydrogen bonding.

In the past, a large number of protein X-ray crystal structures of MbNO and related synthetic model complexes were reported.[13−15] While crystal structures of MbNO have shown that there is a tight range of Fe−NO geometries in low-molecular weight Fe(II)−NO porphyrins, a much wider range of structural parameters were reported for NO−heme protein crystal structures (Fe−NO bond distances in the range of 1.5−2.1 Å and Fe−N−O angles ranging from 112° to 160°).[12,13] The discrepancy between inorganic models and MbNO may be due to two reasons: (i) the distal residues in the heme cavity may play an important role in distorting the geometry of the Fe−NO unit (ii) because of limitations in resolution and structure determination techniques reported structures may be inaccurate. In the protein X-ray structure determination studies, the NO−heme complexes were usually prepared by reactions that took place in the crystal. It has been recently shown that this method of preparation yields different Fe−NO geometries and this suggests that the obtained structures may reflect local rather than global minima.[13] Although, protein crystallography provides the most valuable geometric structure information of MbNO species, their corresponding electronic structures are best probed by advanced spectroscopic techniques such as advanced electron paramagnetic resonance (EPR) based methods.[16,17] These techniques have always occupied a central position in bioinorganic chemistry. First, they allow for the selective investigation of metalloprotein active sites and thereby provide detailed information about the structural changes that occur during a given reaction. Second, they provide insight into the unique electronic structures of the active sites, and are therefore an indispensable tool in linking geometric structures to electronic structure to reactivity. Third, spectroscopy lends itself well to obtain time-resolved data either by rapid freeze or single-turnover transient experiments.[18]

Recently, specific attention has been given to the properties of the hydrogen bond to the NO group in the context of its role in NO reduction reactions.[19] In general, heme−NO complexes may be five or 6-fold coordinate. In EPR experiments on six-coordinate NO−hemes, one often observes two distinct species that differ in the symmetry of their g-tensors.[20] Unfortunately, crystal structure analysis does not provide clues as to the identity of these species. Therefore, spectroscopic studies carried out on samples prepared in solutions become highly relevant.[16,17,20−30] In fact, the frozen solution of MbNO is among the most extensively studied NO-heme complexes. The analysis of the continuous wave (CW)-EPR spectra has led to the recognition of two different paramagnetic species. One with rhombic symmetry of the g-tensor ($[g_{xx}, g_{yy}, g_{zz}] = [2.080, 1.979, 1.998]$) was assigned to the "R-form" and the other with axial symmetry ($[g_{\perp}, g_{||}] = [2.041, 1.983]$) assigned to the "A-form".[20] The A-form was found at all temperatures and dominates at room temperature.
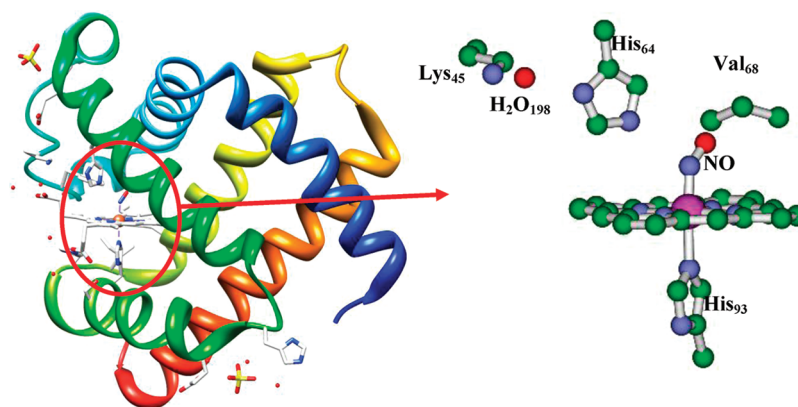
Figure 1. Active site of NO-bound myoglobin. Hydrogens are removed for clarity.

Furthermore, its g-values were found to exhibit small temperature-dependent shifts.[30] The R-form emerges upon cooling, but it is not clearly recognizable at temperatures above 70 K and only at 10−20 K the R-form becomes the dominant contribution to the EPR spectrum.[30] Through comparison of the protein spectra with structurally and spectroscopically characterized model complexes, it was suggested that the observed signals are arising from two six-coordinate conformers of the NO heme nitrogen base complexes, differing primarily in the position of the iron displaced above the heme plane.[25,29] The strong temperature dependence of the EPR spectra of many NO−heme complexes have indicated the existence of a thermal equilibrium between the two forms.[24,25] The interconversion of the A- and R-forms upon decreasing temperature may be induced by protein conformational changes. It was also found that the α-subunits of hemoglobin (Hb) prefers the R-form over the A-form at all temperatures, while β-subunits exhibit an inverted preference much like MbNO. Interestingly, single crystal studies of sperm whale Mb^{15}NO showed that the Fe−NO bond angle is also temperature dependent (153° and 109° at RT and at 77 K respectively).[22] This was deduced from the change of the angle between the directions of hyperfine of ^{15}N(NO) and the g tensor.[22] EPR and ENDOR (electron−nuclear double resonance) studies of single crystals of MbNO revealed only one type of paramagnetic species that is assigned to the R-form.[22,24]

Efforts were directed toward the detection of hydrogen bonds between the distal histidine and the NO. The leading idea is that the conformational changes responsible for the interconversion of the A- and R-forms could be driven by changes in the hydrogen bonding network. Hydrogen bonds involving His64 and Val68 were reported for the two forms using CW X-band ^{1}H ENDOR measurements.[28,29] X-band ESEEM (electron-spin echo envelope modulation) and HYSCORE (hyperfine sublevel correlation spectroscopy) measurements revealed the presence of a weakly coupled nitrogen that was assigned to the distal N$^\varepsilon$ of His64, where the origin of the spin population of the nitrogen atom was attributed to the H-bond with the NO.[26] The assignment of this particular N$_\varepsilon$ to the R- and A-form was, however, ambiguous and it was tentatively assigned to the A-form through correlation with the large ^{1}H hyperfine anisotropy.[26]

Despite all of these efforts, it has still not been determined which factors determine the appearance of the two forms and why in some hemoproteins there only is one form.

Complementary to the significant number of experimental investigations, an equally large number of theoretical studies

devoted to understanding the structure−function relationship of MbNO have appeared in the literature.[31−50] Electronic structure calculations were performed for NO bound porphyrins with variable proximal and distal ligands.[31,35,42−50] Calculations varying from density functional theory (DFT)[31,35,37,39−42,44−46] to correlated wave function based ab initio methods[35,43] were used to understand the geometric and electronic structure, bonding and binding energies[36] of MbNO. In particular, the quality of density functionals toward binding energies of NO to heme systems were assessed and compared to experimental binding energy data (estimated from dissociation barrier of NO from Mb).[51] Compared to the experimental estimates, the hybrid density functionals (such as B3LYP[52,53]) tend to underestimate the binding energies, whereas "pure" functionals (such as BP86[54,55]) tend to overestimate the binding energies of the NO ligand to the heme group.[51] Binding energies calculated with the CASPT2[36] and CCSD(T)[43] methods tend to favor the result that the "pure" functionals deliver. However, severe approximations with respect to the size of the model and the basis set used must be made in order to render these ab initio calculations computationally feasible.

Although a significant number of calculations were performed to probe the structural and electronic differences between different diatomic molecules bound to hemes, only a few studies were devoted to the understanding of the spin-Hamiltonian (SH) parameters of MbNO.[31,35,44,45] Patchkovskii and Ziegler analyzed the g-tensors of a synthetic Fe−NO model complex.[56] They explored the rotational potential energy surface of NO over the heme plane and the sensitivity of the g-tensor to this geometric parameter. Zang et al.[31] carried out Mössbauer calculations using DFT methods and investigated the sensitivity of isomer shift and quadrupole coupling by varying the Fe−NO bond length and Fe−N−O bond angle. Praneeth et al.[44,45] studied the spectroscopic properties and electronic structures of five and six coordinated iron(II) porphyrin NO complexes using a combined experimental and DFT (particularly B3LYP) calculations.[36,37] Serres et al explored the electronic structures for a series of the nonheme Fe-NO using a combined experimental and computational techniques.[35] Zhi et al calculated the magnetic and hyperfine properties of deoxymyoglobin and MbNO using DFT methods.[57]

To the best of our knowledge, no theoretical studies are available that attempt to compute EPR parameters of MbNO in the presence of the protein environment. In fact, such elaborate studies have only recently begun to appear, for example, for

plastocyanin[58] and for cytochrome P$_{450}$.[59] Recently, we reported the combination of advanced pulsed EPR studies on MbNO in conjunction with quantum mechanics/molecular mechanics (QM/MM) studies.[60] In this study, W-band (3.4 T/95 GHz) HYSCORE was used to determine the hyperfine and quadrupole interactions of ^{14}N (proximal histidine) and W-band ^{1}H and ^{2}H ENDOR identified a H-bond to the NO ligand. The combination of theory and experiment allowed for new and experimentally calibrated proposals for the R- and A-forms of MbNO to be put forward.[60]

In this paper, the earlier QM/MM results are elaborated upon. In addition, the following aspects of the MbNO electronic structure are addressed:

(a) What are the geometric differences between the R- and A-forms?
(b) What is the origin of two distinct g-tensors?
(c) How do the neighboring residues, particularly the distal His64, modulate the EPR properties of the R- and A-form?
(d) Which is the most appropriate density functional for the treatment of MbNO? This is of obvious relevance for the treatment of other heme-NO systems and related low-spin Fe-NO systems.

■ COMPUTATIONAL DETAILS

DFT methods provide a way of studying quite large cluster models ($\sim$100–200 atoms), which often may be representative of the electronic structure of the entire protein.[61] However, the appropriate choice of active site model, the choice of density functional and the incorporation of protein dynamics present formidable challenges. On the basis of calibration studies, it has been recognized that the BP86 functional predicts fairly accurate geometries[62] at low computational cost (if the RI approximation[63–66] is used). Hence, it will be used here in conjunction with SV(P) basis set[67–70] for the geometry optimizations reported in this work.

(i). Gas-Phase Calculation Setup. Our model consists of a low spin heme coordinated by His93 and NO. In hydrogen bonding distance to the NO molecule there are Val68 and His64. The latter is hydrogen bonded to a crystallographic water molecule (H$_2$O198), which in turn is hydrogen bonded to a lysine residue (Lys45). Along with the heme and its bound NO, we have included all these amino acid residues in the quantum mechanical (QM) region in order to gauge their importance. The calculations started from the crystal structure of MbNO (PDB Code 2FRJ).[13] Here, the Lys45 is modeled as n-propyl-ammonium ion, His64 and His93 are modeled as methyl imidazole and Val68 as n-propane. Gas phase geometry optimizations were performed using the fragment optimization techniques incorporated into ORCA.[71] In this technique the model is partitioned into six separate fragments (heme with His93 (fragment 1), Lys45(fragment 2), His64(fragment 3), H2O198(fragment 4), nitrosyl(fragment 5), and Val68(fragment 6),

The distance and relative orientation of the fragment pairs of Lys45-heme (fragment 2 to 1), His64-heme (fragment 3 to 1), His64-Val68 (fragment 3 to 6) and Val68-heme (between fragment 1 to 6) are constraint in the optimization while all other degrees of freedom are relaxed. All other fragments (the one which is directly bonded to the heme and NO) are fully optimized and with respect to the other fragments. By this procedure one hopes to incorporate the steric constraints of the protein
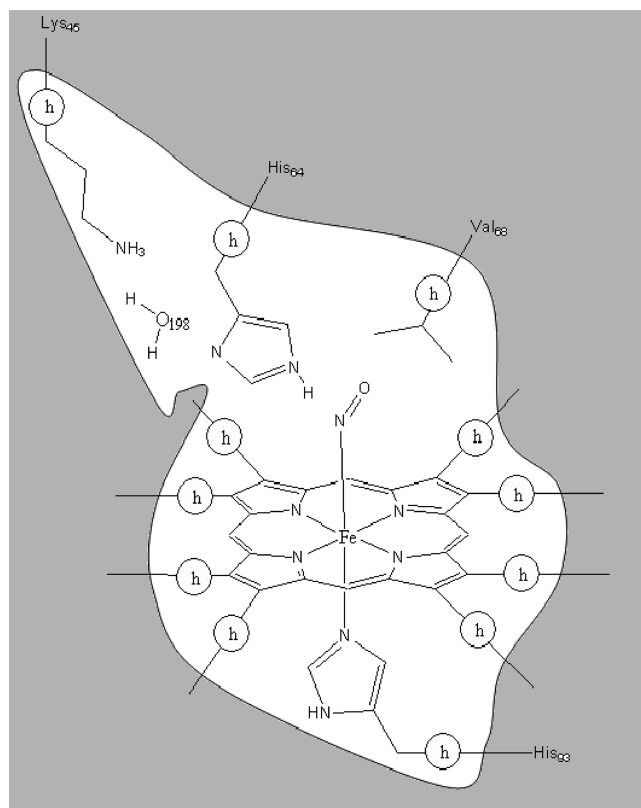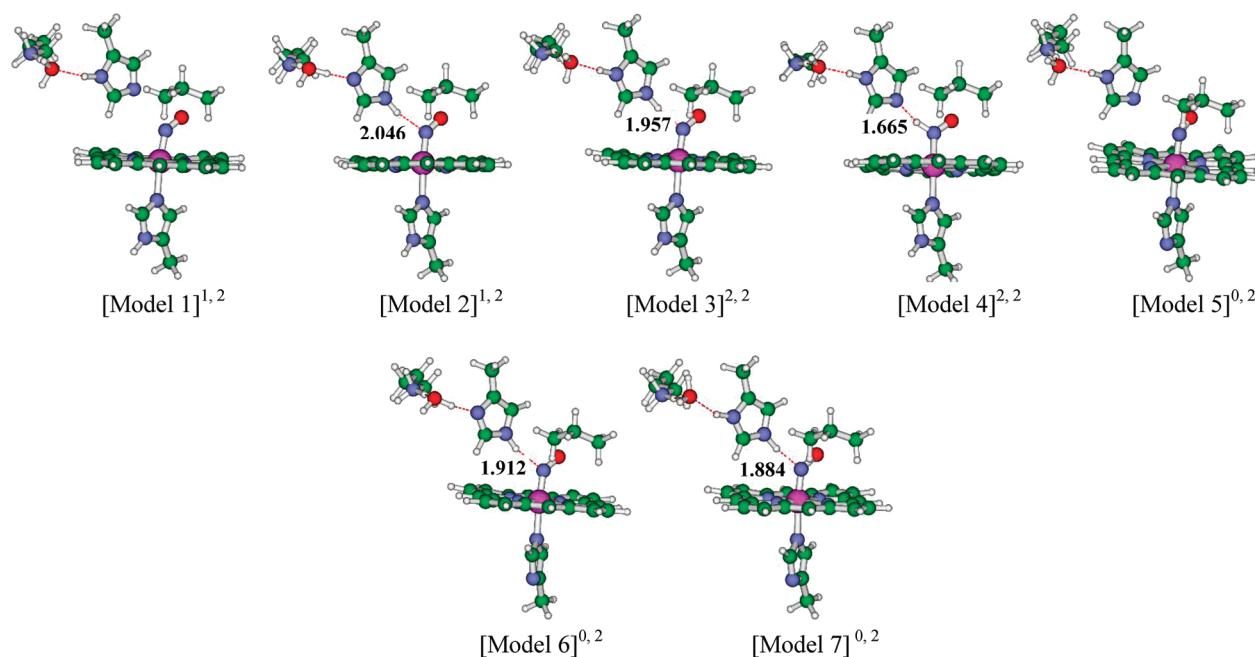

Figure 2. QM/MM partitioning of MbNO of model 2.

pocket in a cluster model. Technically, either the user defines the atoms which make up the connection between the fragments, or the program chooses appropriate atom pairs automatically via a closest distance criterion. Complete details are described in detail in the ORCA manual.[71]

(ii). QM/MM Setup. In the QM/MM calculations, the QM and MM regions were partitioned as follows: His93, His64, and Val68 residues were truncated between C_β–C_α and Lys45 at C_γ–C_β (Figure 2). The heme and the NO group belong to the nonstandard category. We have generated the OPLS-AA force field parameters[72,73] for the heme group using the pro-drg2.5 program.[74] Furthermore, the charges derived by pro-drg2.5 were modified by calculating more accurate electrostatic potential derived charges for the heme and NO groups through the CHELPG algorithm[75] as implemented in ORCA (BP86/SV(P)). The resulting protein model is solvated by $\sim$2600 water molecules. This model was minimized using the steepest descent algorithm by keeping the heme, NO, Lys45, His64, His93, Val68, and H$_2$O198 residues fixed. The minimized geometry was then equilibrated by performing classical Molecular Dynamics (MD) simulations for 100 ps. Finally the relaxed geometries were used in QM/MM calculations. All QM/MM calculations were performed using the ORCA package, which has recently been interfaced to the GROMACS MM package.[76]

(iii). Alternative Models. In proximity of the bound NO, the protonation state of His64 may be crucial, since it may engage in hydrogen bonding with the NO ligand. In Figure 3, we show seven models, which only differ in the protonation states of His93 and His64. In models 1 through 3, His64 is protonated at $N^{\delta 1}$ (model 1) or at $N^{\varepsilon 2}$ (model 2) or at both nitrogens (model 3), whereas, in model 4, the NO ligand is protonated.

[Model 1]^{1,2} [Model 2]^{1,2} [Model 3]^{2,2} [Model 4]^{2,2} [Model 5]^{0,2}

[Model 6]^{0,2} [Model 7]^{0,2}

Figure 3. QM/MM optimized structures. His64 to NO hydrogen bonding distance (Å) is shown. Charge and multiplicity of the seven models are denoted.

For models 5, 6, and 7, His93 is deprotonated with the protonation state of His64 kept similar to models 1 through 3. As Val68 can involve in weak hydrogen bonding to NO,[29] we have chosen Val68 in our model. The models are chosen such a way that the experimental hyperfine coupling of ~10 MHz arises from protons attached to which amino acid residue in close proximity to the FeNO system.

(iv). EPR Calculations. For the calculation of EPR parameters, we use a variety of density functionals including BLYP,[53,54] BPW91,[53,77−81] OLYP,[82] BP86,[54,55] PBE,[83] PBE0,[84] B3LYP,[52,53] O3LYP,[85] and TPSSh.[86] For these calculations, we used CP-(PPP) (for Fe),[87,88] EPR-II[89] (for all nitrogens- and for O of NO) while the remaining atoms were treated with the SV(P) basis set (overall, the calculations included 92 atoms (model 3) in the quantum region).

Nuclear quadrupole coupling constants e^2Qq/h (NQCs) of ^{14}N nuclei were calculated from the electric field gradients V employing a nuclear quadrupole moment $Q(^{14}N)$ of 0.02 barn. In addition, the asymmetry parameters of the quadrupole tensors were calculated as $\eta = (V_{xx} - V_{yy})/V_{zz}$ in a coordinate system with $|V_{zz}| \geq |V_{yy}| \geq |V_{xx}|$.

EPR properties were predicted using coupled perturbed Kohn−Sham theory for the g-tensor[90,91] and the spin−orbit coupling (SOC) operator was treated by spin−orbit mean-field (SOMF) approximation to the Breit−Pauli operator in the implementation of ref 90. Fermi contact terms and spin-dipole contributions to the hyperfine coupling contributions were obtained as expectation values over the ground state spin density. First-order hyperfine couplings were calculated for ^{1}H and ^{14}N, while spin−orbit contributions[91] were taken into account for Fe.[88]

■ RESULTS AND DISCUSSION

(i). Gas-Phase Geometries. We first compare the important geometric parameters of BP86 optimized structures of seven

models in gas phase and in protein (Table 1). We note that, in gas phase geometry optimizations of models 2 and 6, a proton transfer occurs spontaneously from Lys45 to His64, which effectively renders His64 doubly protonated. Further, for all gas phase optimized structures, except model 4, we generally find Fe−NO bond lengths that are shorter than the values experimentally deduced from X-ray diffraction by ~0.1 Å. For model 4, the substrate HNO moiety is somewhat weakly bound (1.85 Å) as the backbonding of NO to Fe is greatly reduced due to protonation.[35] Similarly, the Fe−N−O bond angle of model 4 is somewhat shorter (by 20°) compared to other models and to the X-ray structure. Due to the anionic nature of His93 in Models 5−7, the Fe-NHis93 distance is shorter (~0.1 Å) compared to Models 1−4. Protons of His64 were found to be involved in hydrogen bonding with NO.

(ii). QM/MM Geometries. Compared to gas phase cluster models, we find some significant geometric changes when protein environment are incorporated via QM/MM method. Unlike in gas phase geometry optimizations, we find that for both Model 2 and Model 6 that proton transfer from Lys45 to His64 does *not* take place. In fact, even if the starting geometry featured a doubly protonated His64 it was found that the proton moves back to Lys45. This is expected as the gas phase proton affinity of lysine is much larger than that of histidine (by 10 kcal/mol).[92] We have calculated the pK_a of Lys45 and His64 of the MbNO protein (PDB code: 2FRJ) using the online program, H++pK_a.[93] The calculated pK_a values of Lys45 of His64 are 10.8 and 0.8 units respectively which suggest that Lys45 should be protonated and His64 should be deprotonated, consistent with the QM/MM results.

To understand the discrepancy between the QM/MM and gas-phase geometries present in model 2, we have carefully inspected the neighboring amino acid residues in the proximity to Lys45. We note that Asp60, a propionate of heme and a water molecule (H₂O213) are within three Ångström distance with

Table 1. Important Geometric Parameters of NO-Bound Myoglobin in Gas Phase and in Protein

| models	Fe—N$_{NO}$ (Å)	Fe—N$_{His93}$ (Å)	Fe—N$_{porphyrin}$ (Å)	N—O$_{NO}$ (Å)	Fe—N—O (deg)
			model 1		
gas phase	1.733	2.160	1.994−2.059	1.180	140.8
QM/MM	1.728	2.174	1.999−2.035	1.188	138.2
			model 2		
gas phase					
QM/MM	1.724	2.177	1.995−2.037	1.196	139.3
			model 3		
gas phase	1.749	2.124	2.006−2.054	1.199	137.1
QM/MM	1.737	2.176	2.003−2.031	1.201	136.9
			model 4		
gas phase	1.852	2.073	1.994−2.043	1.212	126.2
QM/MM	1.825	2.123	1.998−2.036	1.217	126.9
			model 5		
gas phase	1.724	1.992	2.014−2.058	1.174	149.0
QM/MM	1.734	2.119	2.005−2.035	1.189	141.4
			model 6		
gas phase					
QM/MM	1.742	2.118	2.001−2.030	1.200	138.1
			model 7		
gas phase	1.779	2.028	2.011−2.047	1.207	136.4
QM/MM	1.757	2.121	2.005−2.036	1.208	136.1
experiment	1.872	2.080	2.040−2.068	1.199	144.1
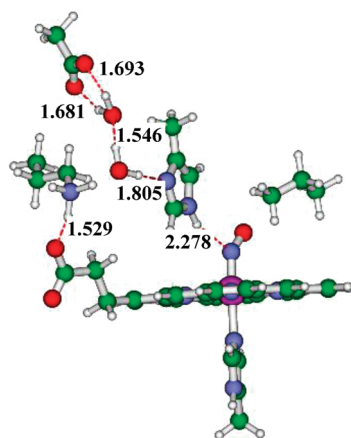
[Model 2]$^{-1, 2}$

Figure 4. Gas-phase geometry optimized structure of the larger model. Charge and multiplicity of the model is denoted.

respect to Lys45. Hence we have carried out a gas phase calculation with a larger cluster model that includes these residues (112 atoms). The larger model gas phase optimized structure is consistent with the QM/MM geometries derived from the truncated model (90 atoms). We note that in the gas phase optimized structure, no spontaneous proton transfer has takes place from Lys45 to His64 because of the extended hydrogen bonding interactions present between Ly45 with the neighboring residues (see figure 4). In QM/MM, the QM region

only "sees" Asp60, H$_2$O213 and propionate via MM point charges. Hence, no spontaneous proton transfer can take place. Thus, larger gas phase clusters including a significant part of the second coordination sphere are necessary to replicate the QM/MM results.

Further, compared to the gas phase results, QM/MM calculations predict a somewhat longer Fe−NHis93 bond distance and a correspondingly shorter Fe−NO bond distance (Table 1). Similar to the gas phase, for all models except model 4, the computed N−O bond distance and Fe−N−O bond angle using QM/MM are in good agreement with the experimental data of a nonprotein complex.[15]

We note that as compared to models 1−3, the Fe−NHis93 distance is shorter by 0.05 Å in models 5−7 due to the anionic nature of NHis93, which leads to a correspondingly small increase in Fe-NO bond distances. Further, in these three models, gas phase Fe−NHis93 bond lengths are shorter by ∼0.1 Å as compared to QM/MM structures due to the lack of steric constraints in the gas phase geometry optimizations (Table 1).

We find that model 2 and model 6 are relatively more stable as compared to model 1 and model 5 by ∼15 kcal mol^{-1}, due to the favorable hydrogen bonding interactions between NO and His64. However, Model 3 and model 4 are nearly iso-energetic. Hence, at the present level of modeling we cannot conclusively deduce which species is favored.

Upon excluding model 4, where NO is protonated, our calculated Fe−NO bond distance is too short compared to experiment. Nevertheless, the predicted geometries of all models (except model 4) are consistent with the high-resolution X-ray

Table 2. Calculated Spin State Energetics (kcal mol^{-1}) of Fe−P−MeIm^{b,a}

		this work	ref 36	ref 43
BP86	S = 0	0	0	0
	S = 1	+0.7	−0.8	+2.4
	S = 2	+10.9	+8.7	+12.9
B3LYP	S = 0	0	0	0
	S = 1	−8.2	−8.9	−4.8
	S = 2	−6.9	−9.6	−4.3
PBE	S = 0	0		
	S = 1	+0.9		
	S = 2	+11.1		
BP86-D	S = 0	0		
	S = 1	+3.5		
	S = 2	+14.6		
B3LYP-D	S = 0	0		
	S = 1	−5.7		
	S = 2	−6.0		
PBE-D	S = 0	0		
	S = 1	+2.1		
	S = 2	+15.2		
CASPT2	S = 0		0	
	S = 1		−6.4	
	S = 2		−16.3	
CCSD(T)^c	S = 0			0
	S = 1			−17.3
	S = 2			−30.4

^{a} Calculations labeled with "-D" contain an empirical dispersion correction as explained in the text. ^{b} P = porphyrin, MeIm=Methyl imidazole. ^{c} Truncated model.

Table 3. Computed Binding Energies (kcal mol^{-1})

		this work	ref 36	ref 43	experiment
Fe−P−MeIm/ gas phase	BP86	46.5	42.7	50.8	
	PBE	49.2			
	B3LYP	11.9	7.3	14.1	
	B3LYP-D	15.1			
	PBE-D	55.3			
	BP86-D	53.2			
					22.8
	CASPT2		21.6		
	CCSD(T)			20	
Model 2/QM/MM	BP86	50.1			
	PBE	53.7			
	B3LYP	14.7			

Figure 5. Sensitivity of g-tensors of model 2 with different density functionals.
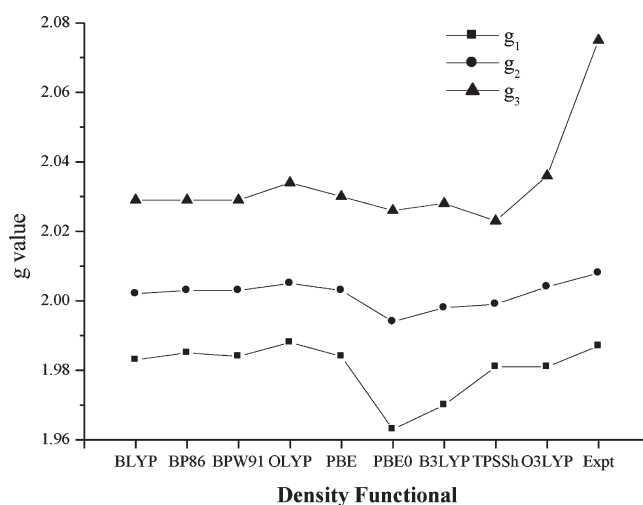
geometry of a closely related synthetic model.[15] One may be tempted to speculate that the main source of the discrepancies between the protein and the synthetic model (as well as the theoretical data) may be due to (i) the presence of hydrogen bonding between NO and His64, Val68 in the protein, (ii) protein strain and electrostatics, but also (iii) possible inaccuracies in the protein structure. The latter problems are typical for protein X-ray structures when small diatomic molecules bind to metalloproteins.[94] In favor of our geometry it is noted that in the QM/MM model, we have included: (a) all important hydrogen bonding residues (His64 and Val68, table 2) and (b) steric and electrostatics effects. It is (c) known that the employed density functional (BP86) tends to predict accurate geometries.[62] The computed geometries can be criticized for using medium sized basis set and excluding relativistic effects. We have addressed this problem by optimizing the structure of Model 2 with a larger basis set (TZVP)[95,96] under inclusion of scalar relativistic effects (ZORA).[97] We conclude that our computed geometric parameters are not particularly sensitive to either choice.

QM/MM calculations predict somewhat stronger hydrogen bonds as compared to the gas phase. Hydrogen bonding between His64 and NO is stronger in models 3 and 7 as compared to models 2 and 6 due to the differing positive nature of His64 (Figure 3). The strength of this hydrogen bond is reflected in somewhat weaker Fe−NO bond lengths in models 3 and 7.

(iii). Choice of Density Functionals and Discussion of the R-Form. The electronic structures of Fe−NO complexes are known to be complicated and challenging to describe by quantum chemical methods.[35,36,45] As the spin density distribution in these systems is crucial for accurate prediction of EPR parameters it is necessary to discuss this subject in some detail. Using the truncated models (90 atoms) our gas phase calculations we are unable to find any minimum energy structures for model 2 and model 6. Hence, in the forthcoming sections, we restrict our results to QM/MM calculations. In addition to the popular B3LYP functional, we used a wide variety of density functionals to assess the prediction of EPR parameters in comparison to the most recent high-resolution experimental data on MbNO.[60] A series of GGA functionals (BLYP, BP86, BPW91, OLYP, PBE), hybrid functionals (PBE0, B3LYP, O3LYP) and a meta-GGA functional (TPSSh) were investigated by computing EPR parameters for all the seven models in the QM/MM framework. The calculated EPR parameters were compared to experimental results for the g-tensor and the HCC of ^{14}N of NO, His93, and ^{1H}His64.

The computed g-tensors of the seven models at the QM/MM level using different functionals are given in table 3. Of all the functionals used here, we generally find that the g-values are heavily underestimated by both the PBE0 and B3LYP functionals

568

dx.doi.org/10.1021/ct200401q | J. Chem. Theory Comput. 2012, 8, 563–574

(Table S1, Figure 5). However, all nine functionals underestimate the g_3 value for all models. This underestimation of g_3 is attributed to limitations of the density functionals for magnetic response properties and is not unusual.[91,98] The meta-hybrid GGA functional TPSSh does not lead to any improvement, in agreement with recent calibration results.[99] In models 2, 3, 6, and 7, the calculated g_3 values are larger than in Models 1 and 5, presumably because of hydrogen bonding (Figure 3). We note that in both models 3 and 7, the hydrogen bonding interactions between His64 and NO are stronger than in models 2 and 6, which is mirrored in the calculated g-values (Table S1). All three calculated g-values (g_1, g_2, and g_3) of model 4 are larger than the free electron value and hence this structure is completely inconsistent with the experimental data and can be ruled out. Thus, on the basis of the computed QM/MM g-tensors, all models except model 4 are potential models for R-form. Hence, more insight may be obtained from the computed hyperfine couplings.

In Table S2, the isotropic nitrogen hyperfine coupling constants (HCCs, A_{iso}) of ^{14}NHis93 and ^{14}NO and the largest proton HCC of His64 (^{1H}His64A_3) are reported. It is expected the ligand HCCs are easier to predict than the g-tensor or the metal HCCs, because the core-level spin polarization is not as pronounced for the light elements, and the spin orbit coupling (SOC) contributions are negligible. The quality of the calculations is judged by calculating these HCCs for all seven models with different density functionals and comparison of the results to the experimental values for the R-form (Table S2).

The calculated ^{14}NO HCCs decrease in the following order: model 1 > model 2 > model 3. Again, this trend is attributed to increased hydrogen bonding interactions upon going from model 1 to model 3. From Table S3 it is obvious that increased hydrogen-bonding interactions with His64 decrease the spin population on NO and hence the calculated $^{14NO}A_{iso}$ is smaller for model 3 than for model 1. Similar trends are also observed for models 5−7, where $^{14NO}A_{iso}$ of model 7 has a smaller value than model 5 for $^{14NO}A_{iso}$. From table S3, it is seen that hydrogen bonding leads to a shift of spin population from the NO group to the central iron.

Except for model 4, the calculations with any of the tested density functionals predict significant values for ^{14N}His93A_{iso}. This value is larger for model 1 than for model 2 and model 3, for which the predicted spin populations decrease in the following order: model 1> model 2> model 3. We predict that the largest component of the HCC tensor of the hydrogen-bonded proton (^{1H}His64A_3) of model 2 is closest to experiment. However compared to other models, this value is more than 10 MHz larger for models 3 and 7, which is inconsistent with experiment. Thus, the strong hydrogen bonding between NO and His64 that is present in these models does not appear to occur in the R form of MbNO.

Taken together, Tables S1 and S2 demonstrate that the calculated g-tensors of models 2, 3, and 7 agree qualitatively with the experimental estimates. However, only for model 2, the calculated nitrogen and proton HCCs are in quantitative agreement with the experimental data. Quite surprisingly, the good agreement with experiment only holds for GGA functionals. Both the B3LYP and PBE0 hybrid functionals severely underestimates $^{14N}A_{iso}$ of NO and His93 (model 2) by ∼10 MHz. We have thus arrived at an experimentally calibrated electronic structure description and will proceed below to analyze the results more closely.

(iv). Spin Populations. From the results presented above, the calculated EPR parameters are very sensitive to the actual models and the choice of functional. The fluctuation in the calculated values can be understood upon studying the spin populations more closely.

Regardless of the density functionals used, an increased spin population on Fe is found for models 2, 3, 4, 6, and 7 compared to models 1 and 5 because of lack of hydrogen bonding in the latter two models (table S3). Compared to Models 2 and 6, in both models 3 and 7, we find more spin population on Fe due to the stronger hydrogen bonding interaction between His64 and NO. This increased hydrogen bonding pattern is mainly due to the positive charge of His64 in the doubly protonated state.

However, as mentioned above, the spin populations are sensitive to the choice of hybrid versus GGA functionals. Functionals without HF exchange (such as BP86, PBE) leading to a preferential spin density flow to iron and hence an electronic configuration that more closely resembles $Fe(I)-NO^+$. Hybrid functionals (with the notable exception of O3LYP) show the opposite behavior which leads to a $Fe(II)-NO\cdot$ like electronic structure description. Obviously, the experimental data favor the former solution.

Praneeth et al[44,45] used magnetic circular dichroism (MCD) spectroscopy coupled to DFT calculations with the B3LYP functional to understand the origin of the different spin distributions in 5- and 6-coordinate Fe−NO model systems. They found that the sixth ligand (nitrogen-donor ligands were investigated) pushes the electrons from Fe to NO. The main conclusion is that the 5-coordinate Fe−NO systems are best described as Fe−(I)−NO$^+$ whereas their 6-coordinate counterparts display a Fe(II)−NO$^\bullet$ like electronic ground state configuration. More recently, Radon and Pierloot[36] calibrated a number of popular density functionals against correlated ab initio methods (CASSCF/CASPT2) and identified the spin populations on Fe−NO systems as a complex problem for quantum chemistry. In agreement with our results, they found that hydrid functionals, such as B3LYP tend to locate more unpaired electrons on the NO unit, whereas nonhybrid functionals(e.g., PBE) tend to localize the spin density more on Fe. The CASSCF method in conjunctions with large basis sets favors the nonhybrid functionals over the hybrid ones. Hence, at the CASSCF level, about 48% and 52% spin population are located on Fe and NO respectively It should be noted that the calculations performed by both Praneeth et al[44,45] and Radon and Pierloot[36] are for model systems and not for the protein itself for which hydrogen bonding significantly alters the spin distribution.

Although direct comparisons cannot be made between our models and earlier reports as the QM models are very different (e.g., they explicitly include hydrogen bonding interactions with NO), we can compare the spin populations of our model 2 structure. Our calculated spin populations on Fe and NO are close to those reported by Radon and Pierloot.[36]

(v). Ab Initio Calculation. To further support our spin density distributions obtained using GGA functionals, we have performed correlated ab initio calculations using the spectroscopy oriented configuration interaction (SORCI[100]) procedure. For these calculations, the QM/MM optimized structure of Model 2 was taken as a basis but truncated in order to make the computations feasible. Thus, we have neglected both the hydrogen bonded residues and point charges. Therefore the model contains only the iron-porphyrin, the axial His93 (modeled as methyl imidazole) and NO. The more accurate def2-TZVPP
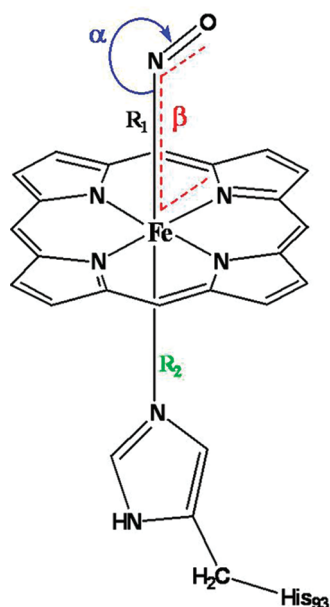
Figure 6. Potential energy surface scan parameters for model 2.

basis[101] was used to describe Fe, def2-TZVP(-f) was used for the directly coordinating nitrogens and NO and the def2-SV(P) basis for the remaining atoms. To facilitate comparison with the SORCI results, DFT calculations (without point charges) using the PBE and B3LYP functionals were carried for the same model and with the same basis sets. As described elsewhere in detail, individual selection was used in order to ease the computational burden.[100] The size of the first-order interacting space was reduced with a threshold $T_{sel} = 10^{-6}$ Eh. A further approximation involves reduction of the reference space through another selection—all initial references that contribute less than a second threshold ($T_{pre} = 10^{-5}$) to the 0th order states are rejected from the reference space.

The initial orbitals for the first step of the SORCI procedure were taken from quasi-restricted orbitals[102] that were further subjected to Pipek—Mezey localization[103] to arrive at a reference space that can be rationally chosen. The average approximate natural orbitals (AANOs), generated from SORCI are shown in Figure 6. In the active space, we have included all five Fe-3d orbitals, two π and two π^* orbitals of NO, and one σ-bonding orbital of the heme group. This leads to an active space of thirteen electrons in 10 orbitals (CAS(13,10), Figure 7).

Using the SORCI wave function, a Löwdin spin population of 75% on Fe is found with 23% of the spin being attributed to the NO group. Thus, the calculated Löwdin spin populations for SORCI and PBE are quite similar thus lending additional support to the plausibility of the PBE result. Thus, the PBE functional was chosen to further investigate MbNO.

(vi). NO Binding Energies. Before discussing structural models for the A-form of MbNO, the calculated binding energies of Model 2 using the B3LYP, BP86 and PBE functionals will be discussed and compared with the experimental estimate of 23 kcal mol^{-1} that was derived from the NO dissociation rate constant.[51]

$$[\text{Me—Im—FeP}] + \text{NO}^\cdot \rightarrow [\text{Me—ImFeP—NO}]$$

For comparison with earlier work of Radon and Pierloot[36] and Olah and Harvey,[43] we have calculated the binding energy for the
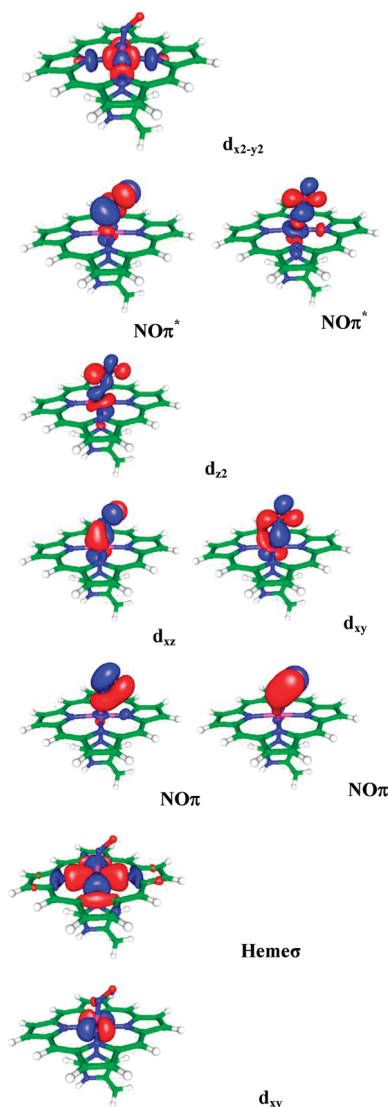

Figure 7. Active natural orbitals of model 2.

truncated model of Model 2 in the gas phase, where the neighboring hydrogen bonding and sterically demanding residues are neglected (His64, H$_2$O198, Lys45, and Val68). For this truncated model, full geometry optimization was performed using the BP86/TZVP. For our large model (Model 2), binding energies were computed using the TZVP basis at BP86/SV(P) preoptimized structures.

The accuracy of the calculated binding energies largely depends upon the correct ordering of the spin states of the five-coordinate heme site. It is important to remember in this context that the substrate (NO) and the NO bound adducts exist in doublet ground states, whereas the empty five coordinate heme site possesses a quintet ground state.[104] We first discuss the calculated spin state energetics and binding energies of NO for the truncated model in gas phase (Table 2). For the five coordinate species, our calculations using the BP86 functional favor a closed-shell singlet ground state with a close lying triplet state and a distinctly high lying quintet state (10.9 kcal mol^{-1}). However, the B3LYP functional predicts a triplet ground state with a close lying quintet state and a high lying singlet state. Hence, the calculated NO binding energy will be sensitive to the
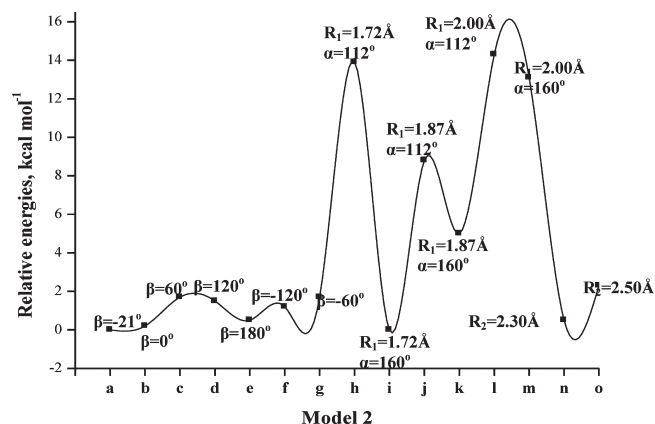
Figure 8. Potential energy surface of model 2.

Figure 9. Sensitivity of g-tensors to geometric variations of model 2.

Figure 10. Sensitivity of HCC's to geometric variations of model 2.

choice of the functional and which spin state we look at. As expected, for the experimental spin state (ground state quintet state for the five coordinate heme site), the BP86 functional will overestimate the binding energy (as the high spin state of the five coordinate heme site is high lying) and the B3LYP functional underestimates it (Table 2). Quite frustratingly, the calculated binding energy using the spectroscopically calibrated PBE functional is significantly overestimated (45 kcal mol^{-1}) despite the fact that this functional is believed to provide the correct electronic structure (Table 3). However, it strongly over binds NO consistent with the well-known tendency of GGA functionals.[36,43] The B3LYP functional on the other hand, while delivering an erroneous electronic structure, underestimates the binding energy NO by a lesser amount (10 kcal mol^{-1}). Our numbers for the truncated gas phase model are in line with the findings of Radon and Pierloot,[36] as well as Olah and Harvey.[43]

It is known that dispersion effects can affect the spin state energetics and the NO binding energies of FeNO systems.[106] Hence, the binding energy calculations were reported with inclusion of the empirical dispersion correction proposed by Grimme.[105] We have evaluated the effect of dispersion contribution to binding energies, without relaxing the geometries at the DFT-D level (BP86-D//BP86). Indeed, the relative spin state energetics are significantly modified (Table 2) for all three functionals by inclusion of dispersion. Although the relative ordering of the spin states is not changed for either the BP86/TZVP nor the B3LYP/TZVP calculations, the singlet state is stabilized by the dispersion correction. For BP86-D/TZVP, the quintet state is $14.6 \text{ kcal mol}^{-1}$ higher in energy than the singlet, resulting in the overestimation of the NO binding energies by 9 kcal mol^{-1}. A similar overestimation is also observed for when PBE-D/TZVP is used. With the B3LYP functional, the incorporation of dispersion corrections improve the binding energies by 4 kcal mol^{-1}. Recently, Siegbahn and co-workers,[106] investigated the effect of dispersion contribution of NO binding to heme-containing model systems. In line with our conclusion, they do find that NO binding energies are significantly improved when dispersion effects are included. They also propose in addition to the dispersion correction, fine-tuning the amount of HF exchange (reducing from 20% to 15%) present in the B3LYP functional (known as B3LYP*) can improve the NO binding energies. Since we mainly focus on spectroscopy here this further degree of freedom was no explored. For the QM/M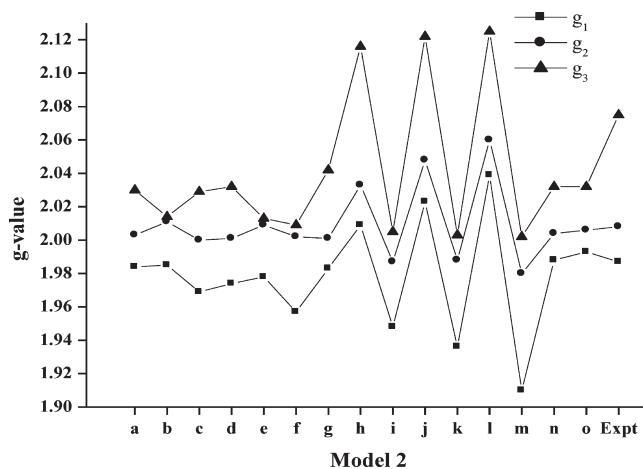M model, the calculated binding energies are slightly larger than in the gas phase truncated model (by 4 kcal mol^{-1}) because of the additional hydrogen bonding interactions that form upon NO binding (compare Figure 2).
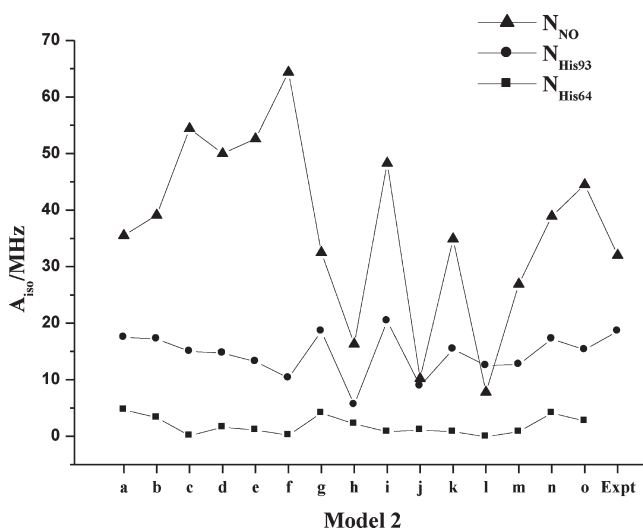
(vii). Potential Energy Surface. On the basis of the discussion above, attention was focused on model 2 and several constraint geometry optimizations were performed to identify the A-form structure (Figure 6). The chosen geometric constraints include: (i) dihedral rotations (β) of the NO with respect to the heme plane (species a–g) (ii) variable Fe–NO bond lengths (R_1) and Fe–N–O bond angles (α) (species h-m) and (iii) differing Fe-His93 bond lengths (R_2) (species o, p). Keeping these minimal constraints, we have optimized all remaining degrees of freedom at the QM/MM level.

We find that both models 2a ($\beta = -21°$) and 2g ($\beta = -60°$) lead to somewhat longer Fe-NO bond distances than Models 2b-2f. This is likely due to strong His64 hydrogen bonding interactions. However based on relative energetics, all models appear to be energetically accessible at room temperature since the potential energy surface (PES) for the dihedral rotation of the NO group over the porphyrin plane is flat ($\sim 2 \text{ kcal mol}^{-1}$, Figure 8). Patchkovskii and Ziegler[56] as well as Zang et al.[31] have performed similar dihedral angle scan calculations in order to understand

571

dx.doi.org/10.1021/ct200401q |*J. Chem. Theory Comput.* 2012, 8, 563–574

the sensitivity of the EPR-g-tensors (but not the HCCs) and Mössbauer parameters upon the geometric variations at the Fe−NO site. Neither study reports QM/MM calculations or includes the second sphere ligands.

As far as Fe−NO bond length and Fe−N−O and bond angle variations are concerned, except for model 2i (R_1 = 1.72 Å and α = 160°) all other species (2h, 2j−2m) are energetically too high (by up to 17 kcal mol^{-1}) to be relevant. The potential energy for bond elongation of the Fe-NHis93 bond (model R_2 = 2n and 2o) by up to 2.50 Å is also flat (the energy increase relative to equilibrium is only ~2 kcal mol^{-1}).

Although the PESs for dihedral rotations of the NO group (species a-g) and the NHis93 bond stretch (species n and o), the EPR parameters for the species involved in the PES are sensitive functions of these geometric parameters (Figures 9 and 10). Thus, even small changes in the Fe−NO bond lengths and Fe−N−O bond angles drastically change the EPR parameters. For example, for a strongly bent Fe−NO bond angle (112°, species 2 h, 2j, 2 L), all three calculated g-values are larger than the free electron value. However for a near linear Fe−NO bond angles (160°, species 2i, 2k, 2m), both g_1 and g_2 fall below the free electron value and the g_3-value is now close to the free electron value. Similarly, at fixed bond angles (112° and at 160°) and when the Fe-NO bond distance is elongated from the optimal value, (1.72−2.00 Å; species 2h, 2j, 2l and 2i, 2k, and 2m), the HCC value of ^{14}NO is decreased and a corresponding increase in ^{14}NHis93A_{iso} is calculated (Figure 10). This is attributed to the stronger Fe−NHis93 interaction. However, at fixed bond lengths with varying Fe−N−O bond angles from bent to linear structure, (compare 2h and 2i, 2j and 2k, 1l and 2m) the ^{14}NO HCC increases dramatically. We also note that Fe−NHis93 elongation from 2.1 to 2.5 Å does not change the HCC of the coordinating nitrogen.

(viii). Potential Models for the A-Form. The absence of a distinct exchangeable H-bonded proton for the A-form could be taken as evidence that (i) there is no hydrogen bonding to NO by His64, (ii) that it has very similar properties to that of R-form such that the two cannot be resolved, or (iii) that it is too small to be observed experimentally. To distinguish between these possibilities, we have calculated the EPR parameters for all the species that are involved in the PES of model 2. The QM/MM calculations showed that an axial g-tensor, where $g_{zz} = g_{xx}$ as observed experimentally, can be obtained for dihedral angles N$_{3(heme)}$−Fe−N−O = 0°, 180° (Figure 9). We have also found a potential R-form structure when the N$_{3(heme)}$−Fe−N−O = −60°. All these three models are energetically within reach (Figure 8).

Similar to the models that lead to a rhombic g-tensor, the calculated g-values of axial symmetry underestimate $g_\perp$. (QM/MM ≈ 2.01 vs exp = 2.03). However, the $g_\parallel$ value is in good agreement with the experimental estimate. (QM/MM = 1.985 vs exp = 1.983, Figure 9) The calculated spin populations of Model 2b and Model 2e on Fe (68%) and NO (30%) are similar to those of the rhombic form (model 2a). Further, the predicted A_{iso} of ^{14}NHis93 (~17.2 and 13.2 MHz) is somewhat smaller in these models than for models Models 2a and 2g. However, the calculated couplings are still substantial as found experimentally (Figure 10). The rotation of the NO group, however, spoils the optimal geometry for H-bonding that was found for the R-form.

We conclude that the most plausible candidate for the A-form of MbNO is a structure that is obtained from the R-form by rotation of the NO group with respect to the heme plane.

The associated PES is fairly flat such that alternative energetic minima are accessible at slightly elevated temperatures (relative to T = 4 K where most EPR experiments are conducted).

■ CONCLUSIONS

In this paper, we used QC methods to gain insight into the bonding and electronic structures of MbNO. In particular, we have assessed the quality of predicted geometries and calculated EPR parameters using contemporary modeling techniques relative to the experimental data.

The treatment is based on the standard QM/MM approach and treats protein effects via MM point charges and a reasonably large QM model (~90 atoms). Our model accounts for important hydrogen bonding (His64) and steric effects (Val68). A number of issues were addressed including possible structural models of the R- and A-forms together with their EPR parameters, selected relaxed PESs. The choice of density functional and the binding energy of NO were also examined.

Of all the models, only model 2 in conjunction with a GGA functional (e.g., PBE), the calculated EPR parameters including g-tensors, ^{14}N HCCs of NO, coordinated His93 and ^{1}H HCC of distal His64 agrees with the recent experimental data.[60] Our calculated spin populations using a GGA functional agree with those of Radon and Pierloot[36] and Olah and Harvey.[43] In addition, the PBE spin populations are close to multireference configuration interaction obtained with the SORCI approach in conjunction with reasonably large basis sets.

The calculated binding energies are sensitive to the choice of density functional. The overestimation and underestimation of NO binding energies to heme using GGA and hybrid functional are largely due to the variable spin state energetics of Fe-heme system prior to NO binding. The use of DFT-D method does improve the results.

Our calculated PESs agree with the earlier studies of Zang et al[31] and Patchkovskii and Ziegler.[56] Changes in the Fe-NO bond length and Fe−N−O bond angle from the equilibrium values are energetically costly. However, the PESs for the NO rotation with respect to NO heme plane and for Fe−NHis93 bond stretch are very flat.

Two possible structural models for A-form of MbNO were proposed. Experimental EPR data suggests that the A-form occurs at slightly elevated temperatures (>77 K), whereas the R-form occurs at cryogenic temperatures. It is conjectured that the A-form arises due to a rotation of the NO molecule that becomes possible at slightly higher temperatures. When the N$_{3heme}$−Fe−N−O dihedral angle is 0° or 180°, the hydrogen bonding interaction of His64 with NO is minimal thus explaining the changes in the spectroscopic parameters that accompany the formation of the A-form.

■ ASSOCIATED CONTENT

ⓢ Supporting Information. Tables of computed g-tensors, computed HCCs, and calculated Mulliken spin populations. This material is available free of charge via the Internet at http://pubs.acs.org.

■ AUTHOR INFORMATION

Corresponding Author
*E-mail: theochem@thch.uni-bonn.de.

572

dx.doi.org/10.1021/ct200401q |*J. Chem. Theory Comput.* 2012, 8, 563–574

■ REFERENCES

(1) Paoli, M.; Nagai, K. In *Handbook of Metalloproteins*; Messerschmidt, A., Huber, R., Poulos, T., Wieghardt, K., Ed.; John Wiley and Sons: Chichester, U.K., 2001.

(2) Ghosh, A.; Steene, E. *J. Biol. Inorg. Chem.* **2001**, *6*, 739.

(3) Williams, R. J. P. *Chem. Soc. Rev.* **1996**, 77.

(4) McCleverty, J. A. *Chem. Rev.* **2004**, *104*, 403.

(5) Richter-Addo, G. B.; Richter-Addo, George B.; Legzdins, P.; Burstyn, J. *Chem. Rev.* **2002**, *102*, 857.

(6) Cheng, L.; Richter-Addo, G. B. In *The Porphyrin Handbook*; Kadish, K. M., Smith, K. M., Guilard, R., Eds.; Academic Press: San Diego, CA, 2000; Vol. 4, Chapter 33.

(7) Xue, L.; Farrugia, G.; Miller, S. M.; Ferris, C. D.; Snyder, S. H.; Szurszewski, J. H. *Proc. Natl. Acad. Sci. U. S. A.* **2000**, *97*, 1851.

(8) Wang, J.; Rousseau, D. L.; Abu-Soud, H. M.; Stuehr, D. J. *Proc. Natl. Acad. Sci. U. S. A.* **1994**, *25*, 9110512.

(9) Martí, M. A.; Capece, L.; Crespo, A.; Doctorovich, F.; Estrin, D. A. *J. Am. Chem. Soc.* **2005**, *127*, 7721.

(10) Chen, W.; Druhan, L. J.; Chen, C.-A.; Hemann, C.; Chen, Y. R.; Berka, V.; Tsai, A.-H.; Zweier, J. L. *Biochemistry* **2010**, *49*, 3129.

(11) Rasmussen, T.; Brittain, T.; Berks, B. C.; Watmough, N. J.; Thomson, A. J. *Dalton Trans.* **2005**, 3501.

(12) Einsle, O.; Messerschmidt, A.; Huber, R.; Kroneck, P. M. H.; Neese, F. *J. Am. Chem. Soc.* **2002**, *124*, 11737.

(13) Copeland, D. M.; Soares, A. S.; West, A. H.; Richter-Addo, G. B. *J. Inorg. Bio. Chem.* **2006**, *100*, 1413.

(14) Brucker, E. A.; Olson, J. S.; Ikeda-Saito, M.; Phillips, G. N., Jr. *PROTEINS* **1998**, *30*, 352.

(15) Piciulo, L.; Rupprecht, G.; Scheidt, W. R. *J. Am. Chem. Soc.* **1974**, *96*, 5293.

(16) Usov, O. M.; Choi, P. S-T.; Shapleigh, J. P.; Scholes, C. P. *J. Am. Chem. Soc.* **2006**, *128*, 5021.

(17) Goldfarb, D.; Lipkin, Y.; Potapov, A.; Gorodetsky, Y.; Epel, B.; Raitsimring, A. M.; Radoul, M.; Kaminker, I. *J. Magn. Reson.* **2008**, *194*, 8.

(18) Boll, M.; Fuchs., G.; Lowe, D. J. *Biochemistry* **2001**, *40*, 7612.

(19) Xu, C.; Spiro, T. G. *J. Biol. Inorg. Chem.* **2008**, *13*, 613.

(20) Morse, R. H.; Chan, S. I. *J. Biol. Chem.* **1980**, *255*, 7876.

(21) Van Doorslaer, S.; Desmet, F. *Methods Enzymol.* **2008**, *437*, 287.

(22) Hori, H.; Ikeda-Satio, M.; Yonetani, I. *J. Biol. Chem.* **1981**, *256*, 7849.

(23) LoBrutto, R.; Wei, Y. H.; Mascarenhas, R.; Scholes, C. P.; King, T. E. *J. Biol. Chem.* **1983**, *258*, 7437.

(24) Kappl, R.; Huttermann, J. *Isr. J. Chem.* **1989**, *29*, 73.

(25) Huttermann, J.; Burgard, C.; Kappl, R. *J. Chem. Soc., Faraday Trans.* **1994**, *90*, 3077.

(26) Tyryshkin, A. M.; Dikanov, S. A.; Reijerse, E. J.; Burgard, C.; Huttermann, J. *J. Am. Chem. Soc.* **1999**, *121*, 3396.

(27) Epel, B.; Arieli, D.; Baute, D.; Goldfarb, D. *J. Magn. Reson.* **2003**, *164*, 78.

(28) Flores, M.; Wajnberg, E.; Bemski, G. *Biophys. J.* **1997**, *73*, 3225.

(29) Flores, M.; Wajnberg, E.; Bemski, G. *Biophys. J.* **2000**, *78*, 2107.

(30) Schmidt, P. P.; Kappl, R.; Huttermann, J. *Appl. Magn. Reson.* **2001**, *21*, 423.

(31) Zhang, Y.; Gossman, W.; Oldfield, E. *J. Am. Chem. Soc.* **2003**, *125*, 16387.

(32) Zhang, Y.; Oldfield, E. *J. Phys. Chem. A* **2003**, *107*, 4147.

(33) Blomberg, L. M.; Blomberg, M. R. A.; Siegbahn, P. E. M. *J. Inorg. Biochem.* **2005**, *99*, 949.

(34) Blomberg, L. M.; Blomberg, M. R. A.; Siegbahn, P. E. M. *J. Inorg. Biochem.* **2004**, *9*, 923.

(35) Serres, R. G.; Grapperhaus, C. A.; Bothe, E.; Bill, E.; Weyhermueller, T.; Neese, F.; Wieghardt, K. *J. Am. Chem. Soc.* **2004**, *126*, 5138.

(36) Radon, M.; Pierloot, K. *J. Phys. Chem. A* **2008**, *112*, 11824.

(37) Hopmann, K. H.; Ghosh, A.; Noodleman, L. *Inorg. Chem.* **2009**, *48*, 9155.

(38) Ghosh, A. *Acc. Chem. Res.* **2005**, *38*, 943.

(39) Wondimagegn, T.; Ghosh, A. *J. Am. Chem. Soc.* **2001**, *123*, 5680.

(40) Rovira, C.; Kunc, K.; Hutter, J.; Ballone, P.; Parrinello, M. *Int. J. Quantum Chem.* **1998**, *69*, 31.

(41) Rovira, C.; Kunc, K.; Hutter, J.; Ballone, P.; Parrinello, M. *J. Phys. Chem. A* **1997**, *101*, 8914.

(42) Linder, D. P.; Rodgers, K. R. *Inorg. Chem.* **2005**, *44*, 8259.

(43) Olah, J.; Harvey, J. N. *J. Phys. Chem. A* **2009**, *113*, 7338.

(44) Praneeth, V. V. K.; Neese, F.; Lehnert, N. *Inorg. Chem.* **2005**, *44*, 2570.

(45) Praneeth, V. V. K.; Näther, C.; Peters, G.; Lehnert, N. *Inorg. Chem.* **2006**, *45*, 2795.

(46) Lehnert, N.; Praneeth, V. K. K.; Paulat, F. *J. Comput. Chem.* **2006**, *27*, 1338.

(47) Silvernail, N. J.; Barabanschikov, A.; Sage, J. T.; Noll, B. C.; Scheidt, W. R. *J. Am. Chem. Soc.* **2009**, *131*, 2131.

(48) Silvernail, N. J.; Barabanschikov, A.; Pavlik, J. W.; Noll, B. C.; Zhao, J.; Alp, E. E.; Sturhahn, W.; Sage, J. T.; Scheidt, W. R. *J. Am. Chem. Soc.* **2007**, *129*, 2200.

(49) Wyllie, G. R. A.; Schulz, C. E.; Scheidt, W. R. *Inorg. Chem.* **2003**, *42*, 5722.

(50) Hayes, R. G.; Ellison, M. K.; Scheidt, W. R. *Inorg. Chem.* **2000**, *39*, 3665.

(51) Olson, J. C.; Phillips, G. N. *J. Biol. Inorg. Chem.* **1997**, *2*, 544.

(52) Becke, A. D. *J. Chem. Phys.* **1993**, *98*, 5648.

(53) Lee, C.; Yang, W.; Parr, R. G. *Phys. Rev. B* **1988**, *37*, 785.

(54) Becke, A. D. *Phys. Rev. A* **1988**, *38*, 3098.

(55) Perdew, J. P. *Phys. Rev. B* **1986**, *33*, 8822.

(56) Patchkovskii, S.; Ziegler, T. *Inorg. Chem.* **2000**, *39*, 5354.

(57) Zhi, Z.; Guenzburger, D.; Ellis, D. E. *J. Mol. Struct. THEOCHEM* **2004**, *678*, 145.

(58) Sinnecker, S.; Neese, F. *J. Comput. Chem.* **2006**, *27*, 1463.

(59) Schoneboom, J. C.; Neese, F.; Thiel, W. *J. Am. Chem. Soc.* **2005**, *127*, 5840.

(60) Radoul, M.; Sundararajan, M.; Potapov, A.; Riplinger, C.; Neese, F.; Goldfarb, D. *Phys. Chem. Chem. Phys.* **2010**, *12*, 7276.

(61) Siegbahn, P. E. M.; Himo, F. *J. Biol. Inorg. Chem.* **2009**, *14*, 643.

(62) Buhl, M.; Kabrede, H. *J. Chem. Theory Comput.* **2006**, *2*, 1282.

(63) Whitten, J. L. *J. Chem. Phys.* **1973**, *58*, 4496.

(64) Baerends, E. J.; Ellis, D. E.; Ros, P. *Chem. Phys.* **1973**, *2*, 41.

(65) Dunlap, B. I.; Connolly, J. W. D.; Sabin, J. R. *J. Chem. Phys.* **1979**, *71*, 3396.

(66) Van Alsenoy, C. *J. Comput. Chem.* **1988**, *9*, 620.

(67) Schafer, A.; Horn, H.; Ahlrichs, R. *J. Chem. Phys.* **1992**, *97*, 2571.

(68) Eichkorn, K.; Treutler, O.; Ohm, H.; Haser, M.; Ahlrichs, R. *Chem. Phys. Lett.* **1995**, *240*, 283.

(69) Eichkorn, K.; Weigend, F.; Treutler, O.; Ahlrichs, R. *Theor. Chem. Acc.* **1997**, *97*, 119.

(70) Eichkorn, K.; Treutler, O.; Ohm, H.; Haser, M.; Ahlrichs, R. *Chem. Phys. Lett.* **1995**, *242*, 652.

(71) Neese, F. *ORCA, An Ab Initio Density Functional and Semiempirical Program Package*; 2007.

(72) Jorgensen, W. L.; Tirado-Rives, J. *J. Am. Chem. Soc.* **1988**, *110*, 1657.

(73) Kaminski, G. A.; Friesner, R. A.; Tirado-Rives, J.; Jorgensen, W. L. *J. Phys. Chem. B* **2001**, *105*, 6474.

(74) Schuttelkopf, A. W.; van Aalten, D. M. F. *Acta Crystallogr., Sect. D: Biol. Crystallogr.* **2004**, *60*, 1355.

(75) Breneman, C. M.; Wiberg, K. B. *J. Comput. Chem.* **1990**, *11*, 361.

(76) Hess, B.; Kutzner, C.; van der Spoel, D.; Lindahl, E. *J. Chem. Theory Comput.* **2008**, *4*, 435.

(77) Perdew, J. P. In *Electronic Structure of Solids '91*; Ziesche, P., Eschrig, H., Eds.; Akademie Verlag: Berlin, 1991; p 11.

(78) Perdew, J. P.; Chevary, J. A.; Vosko, S. H.; Jackson, K. A.; Pederson, M. R.; Singh, D. J.; Fiolhais, C. *Phys. Rev. B* **1992**, *46*, 6671.

(79) Perdew, J. P.; Wang, Y. *Phys. Rev. B* **1992**, *45*, 13244.

(80) Perdew, J. P.; Chevary, J. A.; Vosko, S, H.; Jackson, K. A.; Pederson, M. R.; Singh, D. J.; Fiolhais, C. *Phys. Rev. B* **1993**, *48*, 4978.

(81) Perdew, J. P.; Burke, K.; Wang, Y. *Phys. Rev. B* **1996**, *54*, 16533.

(82) Handy, N. C.; Cohen, A. J. *Mol. Phys.* **2001**, *99*, 403.

(83) Perdew, J. P.; Burke, K.; Ernzerhof, M. *Phys. Rev. Lett.* **1996**, *77*, 3865.

(84) Adamo, C.; Barone, V. *J. Chem. Phys.* **1999**, *110*, 6158.

(85) Cohen, J.; Handy, N. C. *Mol. Phys.* **2001**, *99*, 607.

(86) Tao, J. M.; Perdew, J. P.; Staroverov, V. N.; Scuseria, G. E. *Phys. Rev. Lett.* **2003**, *91*, 146401.

(87) Neese, F. *Inorg. Chim. Acta* **2002**, *337*, 181.

(88) Sinnecker, S.; Slep, L. D.; Bill, E.; Neese, F. *Inorg. Chem.* **2005**, *44*, 2245.

(89) Barone, V. In *Recent Advances in Density Functional Methods, Part I*; Chong, D. P., Ed.; World Scientific Publ. Co.: Singapore, 1996; p 287.

(90) Neese, F. *J. Chem. Phys.* **2005**, *122*, 034107.

(91) Neese, F. *J. Chem. Phys.* **2001**, *115*, 11080.

(92) Bliznyuk, A. A.; Schaefer, H. F, III; Amster, I. J. *J. Am. Chem. Soc.* **1993**, *115*, 5149.

(93) Bashford, D.; Karplus, M. *Biochemistry* **1990**, *29*, 10219.

(94) Sundararajan, M.; Surendran, R.; Hillier, I. H. *Chem. Phys. Lett.* **2006**, *418*, 96.

(95) Schaefer, A.; Horn, H.; Ahlrichs, R. *J. Chem. Phys.* **1992**, *97*, 2571.

(96) Schaefer, A.; Huber, C.; Ahlrichs, R. *J. Chem. Phys.* **1994**, *100*, 5829.

(97) van Wullen, C. *J. Chem. Phys.* **1998**, *109*, 392.

(98) Neese, F. *Magn. Reson. Chem.* **2004**, *42*, S187.

(99) Pantazis, D. A.; Orio, M; Petrenko, T; Zein, S; Bill, E; Lubitz, W; Messinger, J; Neese, F. *Chem.—Eur. J.* **2009**, *15*, 5108.

(100) Neese, F. *J. Chem. Phys.* **2003**, *119*, 9428.

(101) Weigend, F.; Ahlrichs, R. *Phys. Chem. Chem. Phys.* **2005**, *7*, 3297.

(102) Neese, F. *J. Am. Chem. Soc.* **2006**, *128*, 10213.

(103) Pipek, J.; Mezey, P. G. *J. Chem. Phys.* **1989**, *90*, 4916.

(104) Hu, C.; Roth, A.; Ellison, M.; An, J.; Ellis, C.; Schulz, C.; Scheidt, W. *J. Am. Chem. Soc.* **2005**, *127*, 5675.

(105) Grimme, S.; Antony, J.; Ehrlich, S.; Krieg, H. *J. Chem. Phys.* **2010**, *132*, 154104.

(106) Siegbahn, P. E. M.; Blomberg, M. R. A.; Chen, S.-L. *J. Chem. Theory Comput.* **2010**, *6*, 2040.